Long-Range Topological Order in Metallic Glass

Qiaoshi Zeng,[1,2] Hongwei Sheng,[3] Yang Ding,[2] Lin Wang,[2,4] Wenge Yang,[2] Jian-Zhong Jiang,[1]* Wendy L. Mao,[1,5,6] Ho-Kwang Mao[1,2,7]*

Glass lacks the long-range periodic order that characterizes a crystal. In the $Ce_{75}Al_{25}$ metallic glass (MG), however, we discovered a long-range topological order corresponding to a single crystal of indefinite length. Structural examinations confirm that the MG is truly amorphous, isotropic, and unstrained, yet under 25 gigapascals hydrostatic pressures, every segment of a centimeter-length MG ribbon devitrifies independently into a face-centered cubic (fcc) crystal with the identical orientation. By using molecular dynamics simulations and synchrotron x-ray techniques, we elucidate that the mismatch between the large Ce and small Al atoms frustrates the crystallization and causes amorphization, but a long-range fcc topological order still exists. Pressure induces electronic transition in Ce, which eliminates the mismatch and manifests the topological order by the formation of a single crystal.

A crystalline structure is composed of a unit cell that repeats by translational periodicity. In contrast, an amorphous material has far more degrees of freedom and complex configurations [for example, (*1*–*6*)]. It has been established that nominally "disordered" glass structure may still have short-range order (SRO) of the nearest-neighbor atoms (*7*–*9*) that can be visualized by atomic-scale, high-resolution transmission electron microscopy (HRTEM); quantified by radial distribution function using electron (ED), x-ray (XRD), and neutron (ND) diffractions; and analyzed by theoretical simulations. Substantial progress has been made recently in detecting and defining medium-range order (MRO) on length scale longer than the nearest neighbor to several nm [for example, (*6*, *10*–*17*)]. The bond lengths and angles of the clusters in glass may deform, shorten, stretch, and twist relative to their crystalline equivalent, while the topological relationship and connectivity of atoms are conserved (*13*). The SRO and MRO clusters in glass are thus often presented as topologically equivalent to a nanoscale portion (up to nm scale) of a crystal without its rigorous crystalline atomic spacings and bonding angles (*8*, *10*, *13*, *14*, *16*). Whether a glass can have long-range structural order (LRO) close to a crystal, that is, the "perfect glass state" (*16*), has been pursued extensively in open framework glasses, such as ice, silica, and amorphized zeolite (*2*–*4*, *6*, *16*, *18*–*20*), via the route of polyamorphic densification (which is transition between two different amorphous states) resulting from cage collapses. These recent efforts have revealed topological MRO of nm length (*13*) but have not yet discovered LRO.

We have taken an alternative route of studying a close-packed metallic glass (MG) and its polyamorphic densification because of 4f electron delocalization (*21*, *22*). By using single-roller melt-spinning method (*23*), we produced a $Ce_{75}Al_{25}$ MG ribbon with about 1 cm in length (hereafter referred as the *X* direction), 1 mm in width (*Y*), and 20 μm in thickness (*Z*). The amorphous structure of the as-prepared sample was

[1]International Center for New-Structured Materials, Zhejiang University and Laboratory of New-Structured Materials, Department of Materials Science and Engineering, Zhejiang University, Hangzhou 310027, People's Republic of China. [2]HPSynC (High Pressure Synergetic Consortium), Geophysical Laboratory, Carnegie Institution of Washington, 9700 South Cass Avenue, Argonne, IL 60439, USA. [3]School of Physics, Astronomy, and Computational Sciences, George Mason University, Fairfax, VA 22030, USA. [4]State Key Laboratory of Superhard Materials, Jilin University, Changchun 130012, People's Republic of China. [5]Geological and Environmental Sciences, Stanford University, Stanford, CA 94305, USA. [6]Photon Science and Stanford Institute for Materials and Energy Sciences, SLAC National Accelerator Laboratory, Menlo Park, CA 94025, USA. [7]Geophysical Laboratory, Carnegie Institution of Washington, Washington, DC 20015, USA.

*To whom correspondence should be addressed. E-mail: mao@gl.ciw.edu (H.-K.M.); jiangjz@zju.edu.cn (J.-Z.J.)

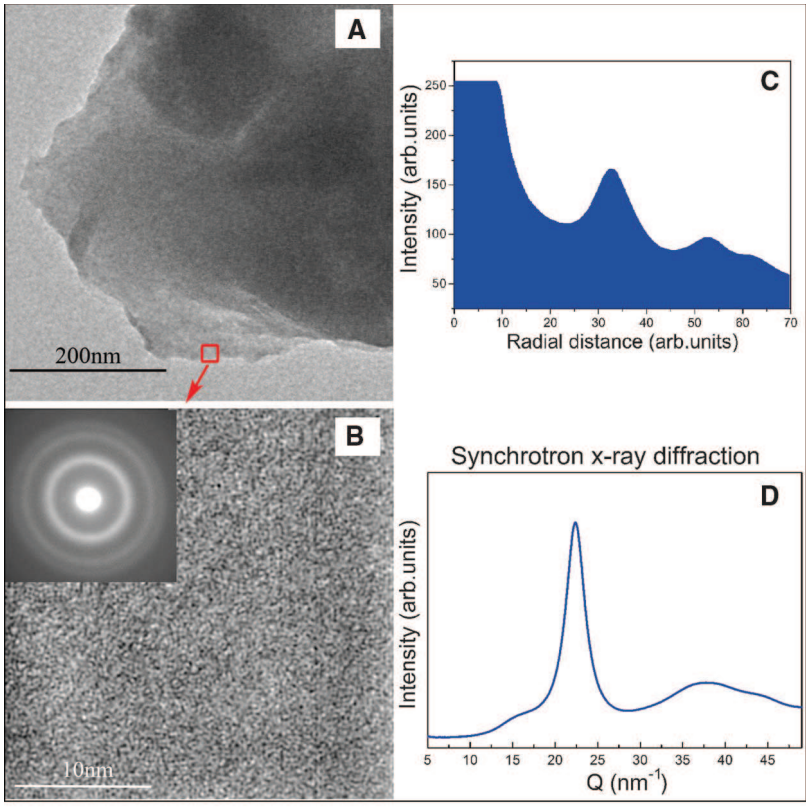

Fig. 1. Structure characterization of the as-prepared $Ce_{75}Al_{25}$ MG ribbon. (**A**) TEM image taken at the Electron Microscopy Center for Materials Research, ANL. (**B**) HRTEM image of the selected thin-edge area shown in the red square of (A). (Inset) ED pattern of the selected area. (**C**) The azimuthal integration of the ED pattern. (**D**) The synchrotron XRD pattern showing the same feature as (C). Diffractions can cover the entire sample but cannot see individual unit cells, whereas HRTEM is capable of resolving unit-cell–sized crystals but can only cover a minute portion of the sample. We searched over 20 randomly picked HRTEM points in the MG to assure a statistically representative imaging. Combination of these diagnostic probes shows that the sample is homogeneous and amorphous. We searched but did not find any microcrystals. Sample preparation for electron microscopy was as follows: The sample was thinned by the mechanical cracking method without any high-energy damaging process as in traditional ion milling and electrical polishing. A thin sliver was scratched off the MG ribbon and dropped into liquid nitrogen. Low temperature embrittled and cracked the sliver into very small flakes, which were dispersed in liquid alcohol and picked up by a copper net for HRTEM analysis.

investigated and confirmed by HRTEM imaging, ED, and XRD analyses (Fig. 1). The MG ribbon was cut into specimens about 50 μm by 40 μm by 15 μm in size. To ensure that we were looking at the internal bulk properties, all six surfaces of the rectangular specimen were recut or polished. A specimen was loaded in a diamond-anvil cell (DAC) along with ruby as the pressure calibrant and helium as the hydrostatic pressure-transmitting medium. In-situ XRD patterns of the $Ce_{75}Al_{25}$ MG at various pressures were collected at synchrotron beamline 16ID-B of the High Pressure Collaborative Access Team (HPCAT), Advanced Photon Source (APS), Argonne National Laboratory (ANL). The sample displayed broad amorphous XRD pattern below 24.4 GPa (Fig. 2). With a slight pressure increment to 25 GPa, the XRD image abruptly and completely transformed to a characteristic spotty zone axis pattern (*24*) of an face-centered cubic (fcc) (*25*) single crystal whose [111] direction coincides with the ribbon length (*X*), and [1$\bar{1}$0], with the ribbon thickness (*Z*). The single crystal (*26*) was preserved after decompressed to the ambient pressure (Fig. 3). Detailed XRD images during compression and decompression are shown in fig. S1.

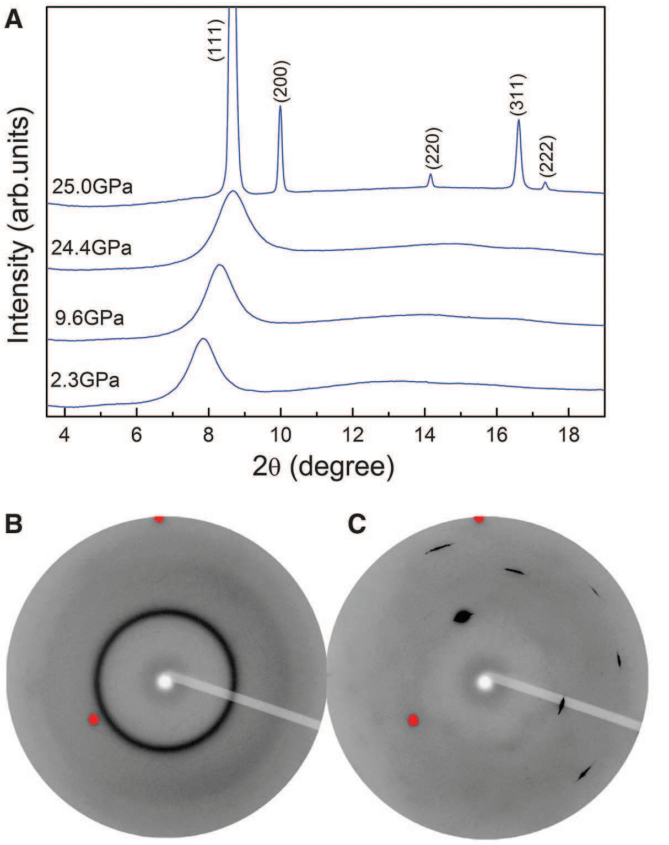

Fig. 2. In-situ high-pressure XRD of $Ce_{75}Al_{25}$ MG in a DAC. (**A**) Integrated XRD patterns, (**B**) two-dimensional (2D) XRD image below 24.4 GPa showing typical glass pattern, and (**C**) 2D XRD image at 25.0 GPa showing typical single-crystal zone-axis pattern (*24*). A focused (15 μm by 15 μm) monochromatic x-ray (wavelength, 0.36806 Å) through the DAC axis without rotation was used for (B) and (C). Red spots are masks of diamond single-crystal XRD spots.

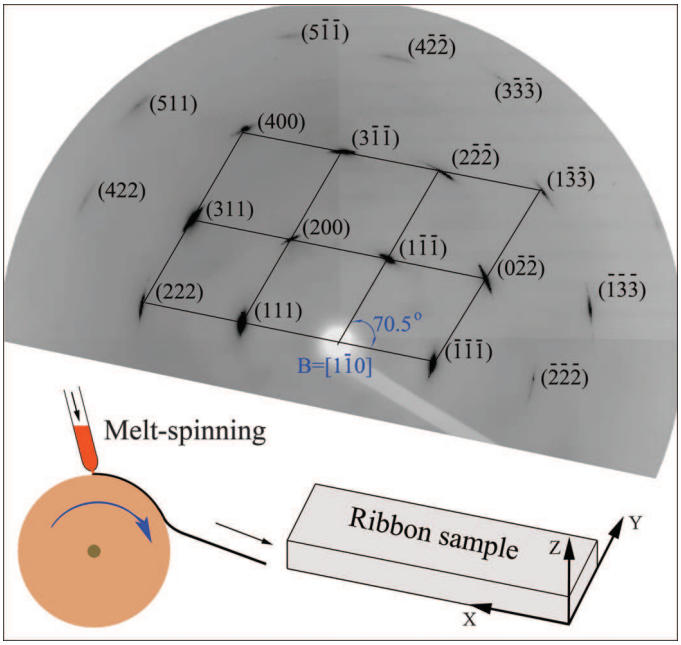

Fig. 3. The 2D XRD image of the fcc single crystal quenched to ambient pressure. The image is indexed as a *Z*-[1$\bar{1}$0] zone-axis pattern with ±5° rotation of the ω axis. The relationship between the crystallographic orientation and ribbon geometry is shown in the schematic illustration.

We observed an invariable orientational relation that the [111] crystallographic direction always formed along the ribbon *X* direction, and [1$\bar{1}$0], along the ribbon *Z* direction over a very long range throughout the entire MG ribbon. We ruled out the possibility of rapid crystal growth originated from a single seed by repeating the experiment with eight different specimens randomly selected from different parts of the same ribbon (fig. S2). Specimens were cut with different surface angles relative to the *X*-*Y*-*Z* axes to test for possible effects of the sample-pressure medium (He) interface and were tilted in the DAC to test for effects of compression direction on crystallization orientation. The strain-free state of the MG was verified (fig. S3), and the stress effect was tested (fig. S4). All tests invariably show the *X* [111]-*Z*[1$\bar{1}$0] relationship upon devitrification in every random unstressed fragment of the MG ribbon. Our observation indicates a topological LRO relationship between structures of the MG and the fcc crystal, without which the nucleation and growth would produce polycrystals of random orientations. At ambient pressure, the stable crystalline phase of $Ce_{75}Al_{25}$ (α phase) has the hexagonal structure that is topologically different from fcc. Indeed, when we devitrified the MG at ambient pressure at 200°C, the product was randomly oriented hexagonal polycrystals. A single crystal is only obtained within the fcc stability field above 25 GPa, demonstrating that the LRO in the MG is uniquely fcc.

The MG must have acquired its LRO during its formation. Both pure Ce and Al crystallize in the fcc structure and have a tendency to produce preferred orientation. The tendency may persist in the random mixture of Ce and Al during the melt-quenching, roller-spinning process. At ambient pressure, the atomic volume of Ce is twice that of Al, and its electronegativity 0.5 lower than that of Al. The extreme mismatch of Ce and Al atoms prevents the formation of a crystalline alloy and results in a glass that shares the common long-range topological relationship with the fcc crystal, but without its long-range spatial periodicity. Such topological LRO will not produce sharp peaks in ED and XRD, which depend on the presence of periodic atomic spacings. This is consistent with the cluster-packing model (*11*, *15*, *21*), which established the fcc symmetry as one of the possible topological MROs in MG. Extension of the topological MRO of the MG to a longer range of many clusters beyond several nm, however, is difficult to quantify by diffraction (fig. S6).

The present observation provides a fresh approach to connect the MRO and LRO through devitrification. Under compression, the Ce atomic volume collapsed because of the 4f electron

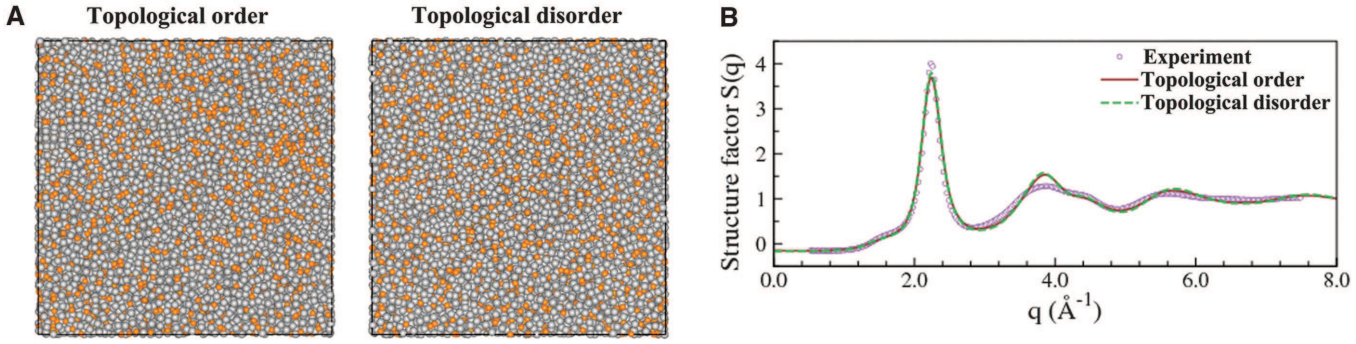

Fig. 4. Computational simulation of $Ce_{75}Al_{25}$ MG structure and XRD patterns at 300 K and ambient pressure. (**A**) Structures of randomly distributed, 3:1 mixtures of Ce (gray spheres) and Al (orange spheres) obtained through two different calculation paths. (**B**) Calculated XRD patterns of the topologically ordered and disordered MGs in comparison to experimentally measured XRD pattern. **q** is the vector of reciprocal space.

delocalization (*21*, *22*, *27*). As the differences of atomic volume and electronegativity between compressed Ce and Al diminish, the Hume-Rothery criteria for crystallization of fcc solid solution are satisfied (*25*). The hidden LRO is then manifested by the pressure-induced devitrification into a single crystal. Although the Ce and its electronic transition provide an unusual opportunity for revelation of the LRO, they are by no means a necessary condition for the LRO itself. $Ce_{75}Al_{25}$ MG does not stand out in the solvent-solute cluster-packing model (*11*, *28*, *29*) among many other MGs that may also have similar topological LRO. In-depth understanding of the $Ce_{75}Al_{25}$ MG case may provide clues for revealing topological LRO in other glasses without the help of Ce.

Is it possible to show explicitly the atomic arrangement of the MG with topological LRO? Is it distinguishable from a MG without the LRO? How could the LRO escape detection by diagnostic probes, for example, HRTEM, ED, and XRD? To address these questions quantitatively, we applied the theoretical methodology (*24*) that has proven successful for other MG systems (*15*, *21*, *30*). We used classical molecular dynamics (MD) calculations using high-fidelity *n*-body interatomic potentials acquired from extensive ab initio calculations (*30*) to simulate the amorphous structure and its evolution through pressure, temperature, and electronic changes. We started by distributing 24,000 Ce and 8000 Al atoms randomly on an fcc lattice at ambient pressure to reflect the tendency of preferred orientation of the quenched melt on the spinning roller. Then we relaxed the lattice constraint and let the simulation proceed. Because of the extreme mismatch between Ce and Al, the atomic positions, coordination numbers, and bonding angles of the fcc alloy automatically deformed, stretched, and twisted, but the topology was basically intact. Finally the fcc lattice was frustrated and transformed to a MG as shown at Fig. 4A, left. This MG, however, still kept hidden memory of the original fcc topology. When the simulation proceeded to high pressures, where the 4f localized Ce transformed to 4f delocalized, the MG became unstable and reverted through a discontinuous transition back to the fcc lattice of the original orientation.

For comparison, we also generated a MG without LRO by quenching a melt directly from 1500 K to 300 K without the fcc constraining step, and the result is shown in Fig. 4A, right. These two structures are practically indistinguishable from each other down to atomic-level resolution, comparable to what would be seen in a HRTEM image. XRD patterns of ordered and disordered MGs were also computed by using MD atomic configurations (Fig. 4B). They show the broad glass patterns indistinguishable from each other and agree with our experimental XRD pattern in peak positions, peak widths, and intensities, reflecting their similarity in SRO and MRO and their absence of long-range spacing periodicity. Diffractions (ED, XRD, and ND) are powerful probes for atomic spacing but are insensitive to topological LRO in glass.

In summary, we observed a pressure-induced devitrification where every portion of a cm-sized $Ce_{75}Al_{25}$ MG ribbon crystallizes independently to the identical orientation, in effect, forming a giant fcc single crystal. We deduced the presence of incipient topological LRO in the glass. Because of the drastic pressure-induced volume collapse of Ce, Ce-Al MG represents an exceptionally favorable system for discovery of the long-sought perfect glass (*1*, *6*, *16*, *19*), which may also exist in other glasses, including many MGs with the similar atomic size disparity and Hume-Rothery frustration as the Ce-Al MG.

References and Notes

1. W. Kauzmann, *Chem. Rev.* **43**, 219 (1948).
2. C. A. Tulk *et al.*, *Science* **297**, 1320 (2002).
3. S.-H. Chen, W.-R. Chen, F. Mallamace, *Science* **300**, 619 (2003).
4. J. L. Yarger, G. H. Wolf, *Science* **306**, 820 (2004).
5. C. A. Angell, *Science* **319**, 582 (2008).
6. G. N. Greaves, S. Sen, *Adv. Phys.* **56**, 1 (2007).
7. J. D. Bernal, *Nature* **183**, 141 (1959).
8. J. C. Phillips, *J. Non-Cryst. Solids* **34**, 153 (1979).
9. W. K. Luo *et al.*, *Phys. Rev. Lett.* **92**, 145502 (2004).
10. J. C. Phillips, *J. Non-Cryst. Solids* **43**, 37 (1981).
11. D. B. Miracle, *Nat. Mater.* **3**, 697 (2004).
12. T. C. Hufnagel, *Nat. Mater.* **3**, 666 (2004).
13. P. S. Salmon, R. A. Martin, P. E. Mason, G. J. Cuello, *Nature* **435**, 75 (2005).
14. P. S. Salmon, A. C. Barnes, R. A. Martin, G. J. Cuello, *Phys. Rev. Lett.* **96**, 235502 (2006).
15. H. W. Sheng, W. K. Luo, F. M. Alamgir, J. M. Bai, E. Ma, *Nature* **439**, 419 (2006).
16. J. Haines *et al.*, *J. Am. Chem. Soc.* **131**, 12333 (2009).
17. D. Ma, A. D. Stoica, X. L. Wang, *Nat. Mater.* **8**, 30 (2009).
18. J. S. Tse, D. D. Klug, J. A. Ripmeester, S. Desgreniers, K. Lagarec, *Nature* **369**, 724 (1994).
19. G. N. Greaves *et al.*, *Nat. Mater.* **2**, 622 (2003).
20. A. Navrotsky, *Nat. Mater.* **2**, 571 (2003).
21. H. W. Sheng *et al.*, *Nat. Mater.* **6**, 192 (2007).
22. Q. S. Zeng *et al.*, *Phys. Rev. Lett.* **104**, 105702 (2010).
23. A. L. Greer, *Science* **267**, 1947 (1995).
24. Materials and methods are available as supporting material on *Science* Online.
25. Q. S. Zeng *et al.*, *Proc. Natl. Acad. Sci. U.S.A.* **106**, 2515 (2009).
26. The single crystal could also be viewed as an aggregate of polycrystals with the identical orientation; in either case, it reveals a LRO in the MG.
27. A. R. Yavari, *Nat. Mater.* **6**, 181 (2007).
28. D. V. Louzguine-Luzgin, A. R. Yavari, G. Vaughan, A. Inoue, *Intermetallics* **17**, 477 (2009).
29. D. B. Miracle, T. Egami, K. M. Flores, K. F. Kelton, *MRS Bull.* **32**, 629 (2007).
30. Y. Q. Cheng, E. Ma, H. W. Sheng, *Phys. Rev. Lett.* **102**, 245501 (2009).

Acknowledgments: This material is based on work funded by the U.S. Department of Energy (DOE), Energy Frontier Research Center grant DE-SC0001057 (EFree). We thank C. L. Qin for synthesis of the MG, B. Sa and Z. Sun for initial calculations, R. E. Cook and R. Koritala for helping ED and TEM measurements, and S. Sinogeikin and Y. Meng for the x-ray beamline support. The use of HPCAT, APS is supported by Carnegie Institute of Washington, Carnegie DOE Alliance Center, University of Nevada at Las Vegas, and Lawrence Livermore National Laboratory through funding from DOE–National Nuclear Security Administration, DOE–Basic Energy Sciences, and NSF. The TEM measurements were conducted at the Electron Microscopy Center at ANL. The computational work was supported by NSF grant DMR-0907325 and conducted on the supercomputing system supported by the Center for Computational Materials Science, Tohoku University. The SLAC effort is supported by DOE and DE-AC02-76SF00515. The Zhejiang University participants are supported by the National Natural Science Foundation of China (grants 10979002, 50920105101, and 51050110136), the China Postdoctoral Science Foundation, the Zhejiang University-Helmholtz Cooperation Fund, the Ministry of Education of China, and Zhejiang Provincial Department of Science and Technology.

Supporting Online Material

www.sciencemag.org/cgi/content/full/332/6036/1404/DC1
Materials and Methods
Figs. S1 to S6
Table S1
References (*31*–*40*)

11 November 2010; accepted 12 April 2011
10.1126/science.1200324

Supporting Online Material for

Long-Range Topological Order in Metallic Glass

Qiaoshi Zeng, Hongwei Sheng, Yang Ding, Lin Wang, Wenge Yang, Jian-Zhong Jiang,*
Wendy L. Mao, and Ho-Kwang Mao*

* To whom correspondence should be addressed: mao@gl.ciw.edu or jiangjz@zju.edu.cn

Fig. S1, S2, S3, S4, S5, and S6; Table S1

Zone-axis patterns for high-pressure, single-crystal, XRD study

The zone-axis XRD pattern is commonly observed and used in single-crystal DAC experiments. It takes advantage of the short-wavelength, monochromatic, synchrotron x-rays (0.36806 Å in the present experiment) and thin sample (~10 μm) to obtain electron diffraction-like pattern on 2-dimension detectors (*30*). When the monochromatic x-ray beam is aligned nearly parallel to a zone axis of the crystals, many diffraction spots associated with the zone axis appear in a single exposure without the need of rotating the single crystal into the Bragg condition, thus instantly providing the *d*-spacing, the unit-cell parameters, the orientation matrix and geometry of the single crystal that are the key information for the present study. In addition to the high efficiency, its benefit over the standard crystal-rotation (perpendicular to the x-ray beam) XRD method is particularly noticeable when the x-ray access aperture is restrictive. Here we used the cubic BN seats which allow ±30° diffraction through the cBN, but the rotation is limited by the hole opening in the seat to ±5°, beyond which the incident x-ray will hit the cBN seat and produce a very strong background from XRD of the polycrystalline cBN and two single-crystal diamonds. Even if we use the Boehler-type wide-angle seats (*31*), the strong diamond XRD is still unavoidable during rotation. Using the zone-axis XRD without rotation, the single-crystal diamond XRD can be avoided or minimized (see the two red masks of the diamond spots in Figs. 2 and S1). The clean background allows us to confirm the complete devitrification to a single crystal and the absence of weak XRD from

amorphous or polycrystalline materials in the specimen.

Unlike the crystal-rotation technique, the zone-axis XRD only shows partial pattern. The relative intensities of different peaks are very sensitive to slight rotation, and cannot be used for structural refinement of the DAC samples. This is not a concern for the fcc structure which does not have a refinable structural parameter. The zone-axis XRD can be combined with a limited rotation in a small range to cover some missing spots. For instance, Fig. 3 shows the zone-axis pattern combined with ±5° rotation to cover the complete pattern in $2\theta = \pm 50°$ for the sample quenched to ambient pressure.

Compression, devitrification, and decompression of the $Ce_{75}Al_{25}$ MG

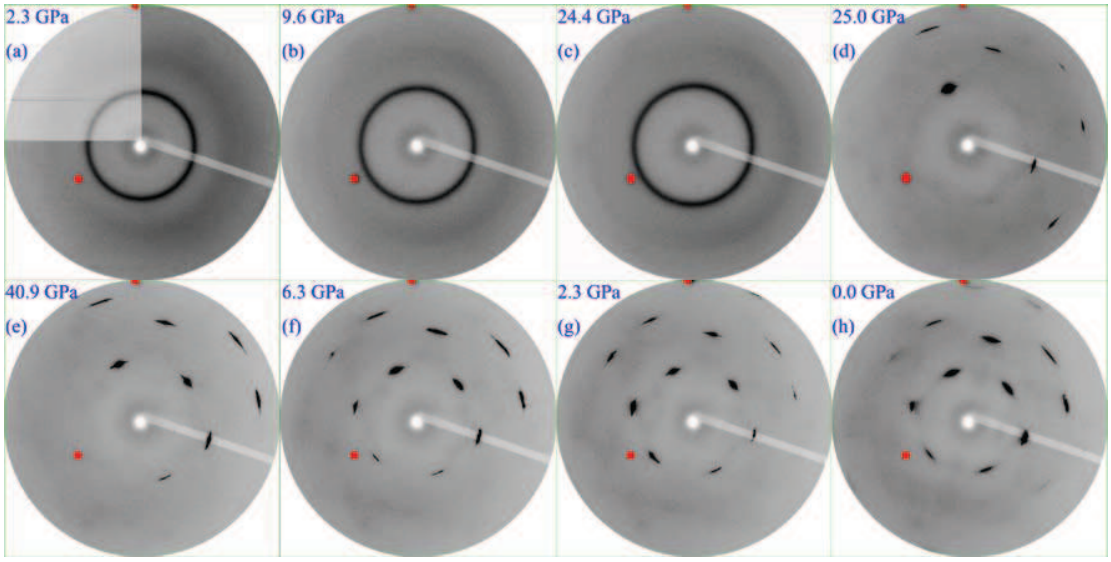

Fig. S1. In-situ high-pressure 2D XRD images of $Ce_{75}Al_{25}$ MG in a DAC; (a) – (c) compression to 24.4 GPa showing typical glass patterns with broad amorphous rings; (d) divitrification at 25.0 GPa showing very intense and sharp single-crystal zone-axis spots without the broad glass rings or sharp polycrystalline rings; (e) continuous compression to 40 GPa, XRD spots shifting to higher angles (smaller *d*-spacings); (f) - (h) decompression to ambient pressure, XRD spots shifting to lower angles (larger d-spacings) but maintaining the same geometry. A focused (15×15 μm^2) monochromatic x-ray (wavelength, 0.36806Å) through the DAC axis without rotation is used for all images. Red spots are masks of diamond single-crystal XRD spots, showing the constant x-ray direction relative to the DAC. The gradual change of relative intensities of spots in the zone-axis pattern reflects slight tilting of the specimen (~1°-2°) during compression and decompression. The integrated XRD patterns of (a) – (d) are plotted and shown in Fig. 2 of the paper.

Table S1. Millers indices and *d*-spacings of all fcc single-crystal spots of the Ce_3Al alloy at ambient pressures (Fig. 3); a_0 = 4.8662(3) Å.

hkl	D_{obs} (Å)	D_{cal} (Å)
111	2.8108	2.8096
$\bar{1}11$	2.8099	
$\bar{1}\bar{1}\bar{1}$	2.8084	
200	2.4349	2.4332
$0\bar{2}\bar{2}$	1.7199	1.7205
311	1.4671	1.4672
$3\bar{1}1$	1.4664	
222	1.4051	1.4048
$2\bar{2}\bar{2}$	1.4043	
$\bar{2}\bar{2}\bar{2}$	1.4049	
400	1.2170	1.2166
$1\bar{3}\bar{3}$	1.1163	1.1164
$\bar{1}\bar{3}\bar{3}$	1.1165	
422	0.9939	0.9933
$4\bar{2}\bar{2}$	0.9930	
333	0.9358	0.9365
511	0.9373	
$5\bar{1}\bar{1}$	0.9365	

Additional characterizations of the $Ce_{75}Al_{25}$ MG

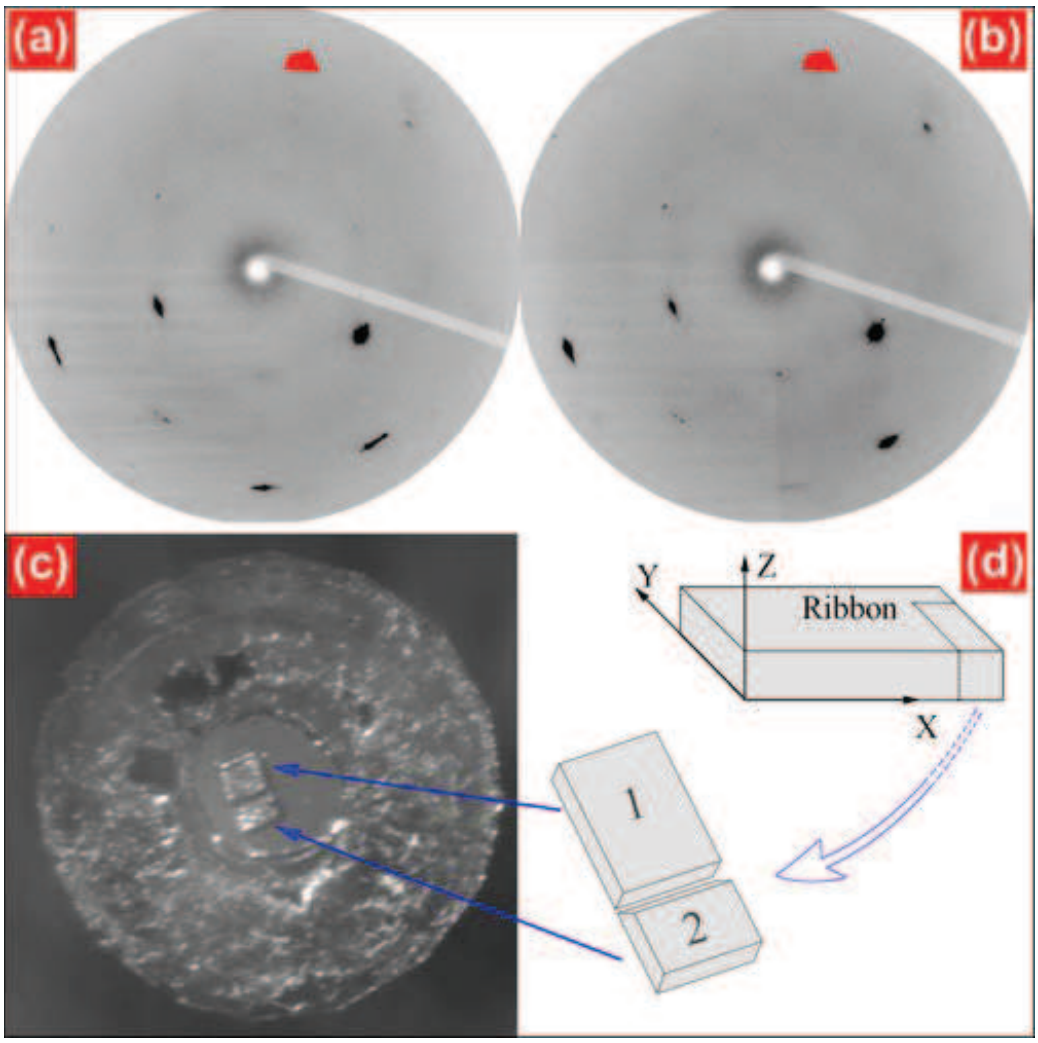

Fig. S2. XRD images of a single specimen cut and separated into two parts. (a) Part 1, and (b) part 2 at 25 GPa showing identical fcc single-crystal zone-axis patterns. Red patches are masks of diamond single-crystal XRD spots. (c) Photomicrograph showing the specimen in a DAC. The diamond culet diameter is 400 μm, part 1 is about 50×40 μm^2, and part 2 is about 30×40 μm^2. (d) Schematic illustration of the two parts relative to the ribbon geometry. The test eliminates the possibility of rapid single-crystal growth from a single nucleus, which cannot cross the gap separating the two parts.

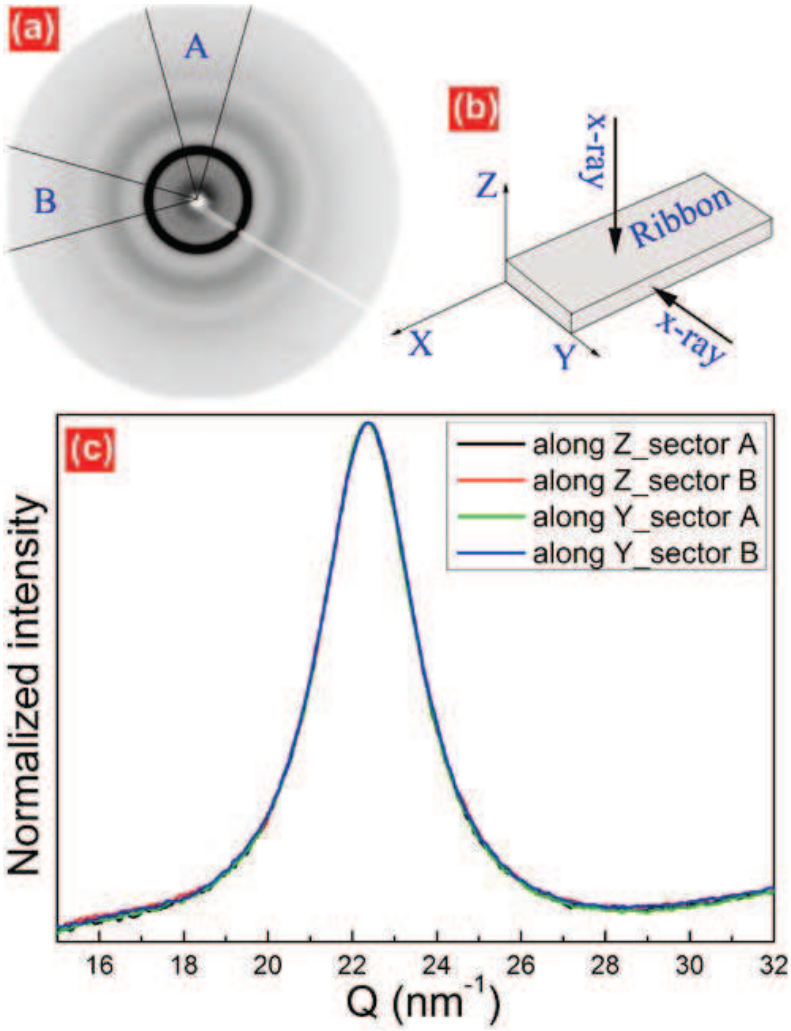

Fig. S3. Structure and strain anisotropy measurements of as-prepared $Ce_{75}Al_{25}$ MG ribbon specimen by XRD image cake method (*32*). (a) A representative 2D XRD image which includes two orthogonal pie-shaped sectors labeled as A and B, with azimuth angle of 30° each. (b) The diffraction geometry with respect to the ribbon directions. We have measured diffraction in X (A sector) and Y (B sector) with incident x-ray along Z, and diffraction in Z (A sector) and X (B sector) with incident x-ray along Y. (c) Comparison of integrated XRD sectors. No difference can be found among the four-sector comparison of the main diffraction peak which is sensitive to small variation in structure and strain, indicating that the strain in as-prepared $Ce_{75}Al_{25}$ MG is below the detection limit.

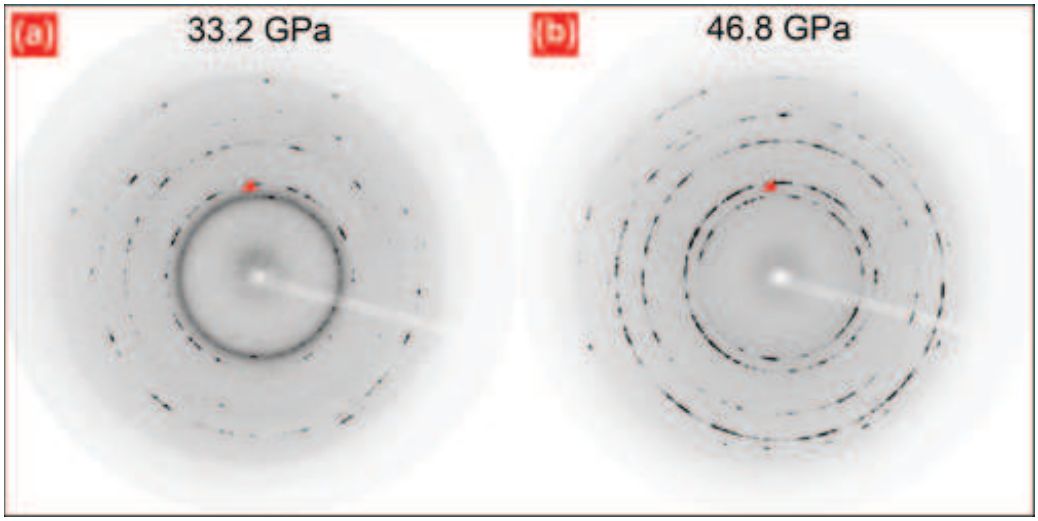

Fig. S4. XRD images of $Ce_{75}Al_{25}$ MG in DAC without pressure medium at two pressures. The MG was severely deformed and its LRO was destroyed under uniaxial stress. Divitrification became sluggish and produced fcc Ce_3Al random alloy polycrystals. As shown by the broad innermost ring, some MG still remained at 33.2 GPa and devitrification completed at 46.8 GPa. Red spots are masks of diamond single-crystal XRD spots. The test indicates that strong uniaxial stress does not facilitate the single-crystal growth, but destroys the condition for single crystal growth.

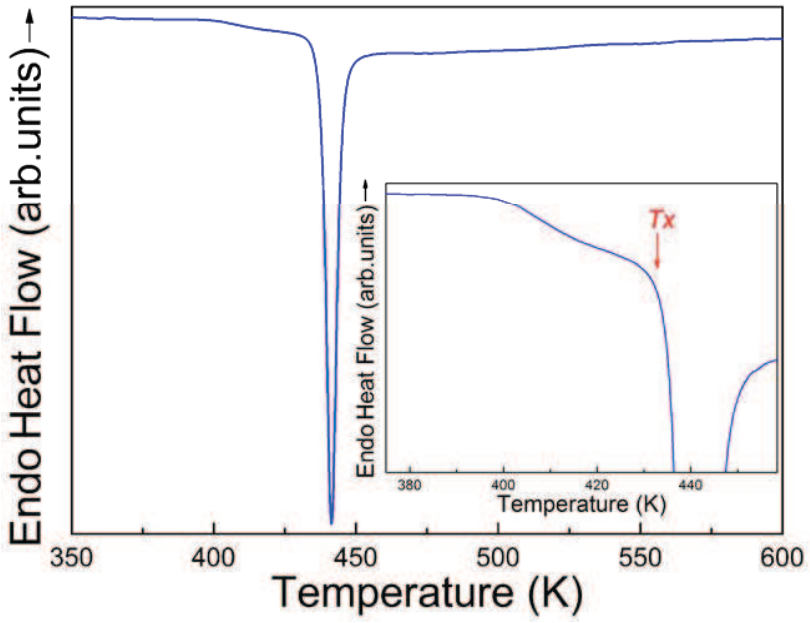

Fig. S5. Differential scanning calorimetry measurement during heating of the $Ce_{75}Al_{25}$ MG specimen . The weak endothermic glass transition signal (the shoulder bump in the inset) in $Ce_{75}Al_{25}$ is similar to that typically observed in Al-based MGs, *e.g.*, (*33, 34*), and is believed to be obscured by both the strong exothermic structural relaxation signal (starts at about 400 K) before the glass transition and the closely followed exothermic crystallization reaction (Tx).

Computational Methods

The embedded-atom-method (EAM) type of interatomic potentials was used for molecular dynamics simulation of Ce-Al MGs. The interatomic potentials were developed by fitting the potential energy landscape (PES) of Ce-Al, which was pre-established through extensive ab-initio calculations based on the density functional theory (DFT) with the Vienna Ab-initio Simulation Package (*35-37*). To construct the PES of Ce-Al, a total of 1600 atomic configurations were included in the DFT database, in which each atomic configuration typically contains 100 atoms. The DFT database was further augmented by incorporating experimental data such as lattice parameters, elastic constants and phonon frequencies of γ-Ce. EAM interatomic potentials for Ce-Al were optimized by using the force-matching method implemented in the Potfit package (*38*).

The as-developed EAM potentials for Ce-Al have been validated against a large array of experimental data. The potentials are found adequate to describe defects, equation of states, elastic constants, mechanical properties and vibrational properties of both Ce and Al, and are also accurate to describe the energetics of various intermetallic phases between Ce-Al. The potentials predict correctly the glass formation temperatures (Tg), the structure factors of Ce-Al MGs, as well as density changes due to the polyamorphic transition of Ce-Al MGs (*21, 22*).

To simulate the formation of $Ce_{75}Al_{25}$ MG, we conducted large-scale molecular dynamics (*39*) employing the as-developed interatomic potentials to monitor the evolution of the glasses through pressures. MD simulations were conducted with NPT ensembles (constant number of particles, pressure, and temperature), and the temperature was controlled using a Nose-Hoover thermostat. Then we relaxed the lattice constraint and let the simulation proceed at 450 K and 5 GPa for 1 ns. Due to the extreme mismatch between Ce and Al, the atomic positions, coordination numbers, and bonding angles of the fcc alloy automatically deformed, stretched, and twisted, but the topology was basically intact.

Revelation of MRO by diffraction experiments and pair correlation function

Ref. (*11*) suggested that the MRO in MG can be revealed from the reduced partial pair correlation functions (PCF) up to about 1.5 nm. In order to interpret the exact type of MRO in MG based on experimental PCF data, other analytical techniques, such as Reverse Monte Carlo (*15*), are found useful. In the present work, it is tempting to relate the long-range atomic order to their PCF data. The following figure demonstrates the reduced total and partial PCFs of the Ce-Al MG with LRO (see Fig. 4, text), as obtained from molecular dynamics simulations.

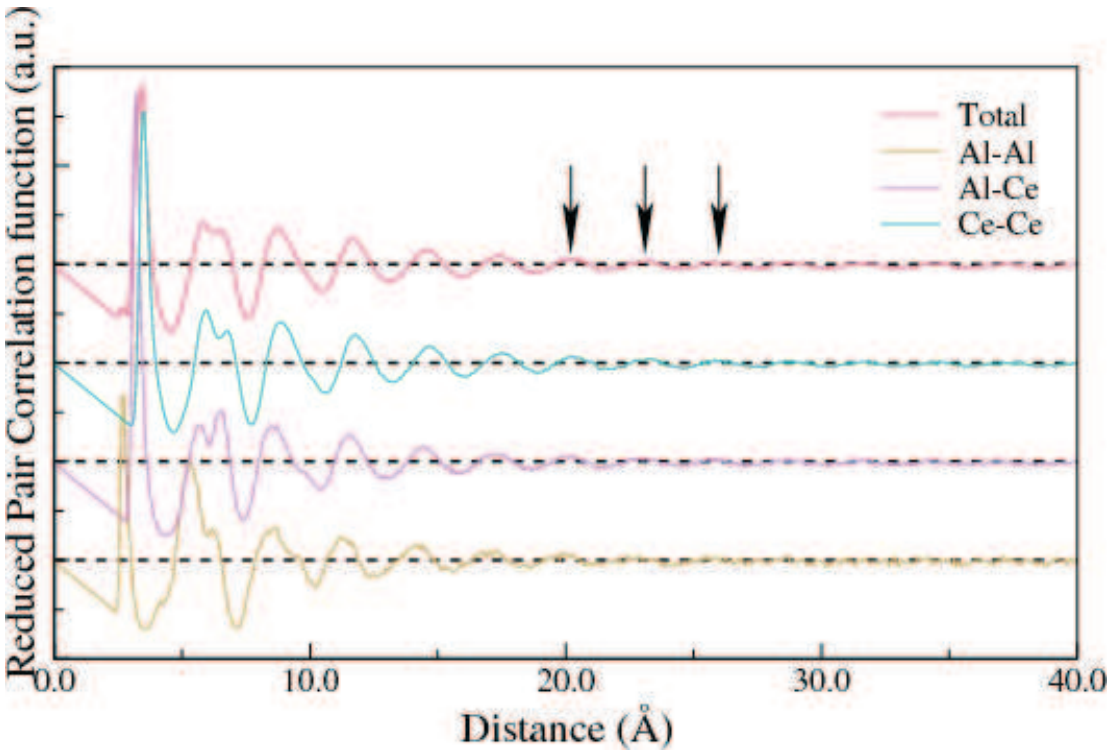

Fig. S6. Pair-correlation peaks are identifiable up to 2.7 nm (indicated by the arrows), indicating an atomic packing order that goes beyond a few atomic shells as characterized by MRO (~1.5 nm, (*14*)), and extends into longer range. Experimentally, however, it remains to be demonstrated whether modern diffraction techniques are capable of revealing the correlations at such an interatomic distance. It should be mentioned that when the long-range correlation length is larger than 2.7 nm, the reduced PCFs are inadequate to

describe the LRO inherited in the structure. High-order correlation functions, such as orientational order parameter, may be found useful in characterizing the LRO.

References and Notes

1. W. Kauzmann, The nature of the glassy state and the behavior of liquids at low temperatures. *Chem. Rev.* **43**, 219 (1948). doi:10.1021/cr60135a002

2. C. A. Tulk *et al*., Structural studies of several distinct metastable forms of amorphous ice. *Science* **297**, 1320 (2002). doi:10.1126/science.1074178 Medline

3. S.-H. Chen, W.-R. Chen, F. Mallamace, The glass-to-glass transition and its end point in a copolymer micellar system. *Science* **300**, 619 (2003). doi:10.1126/science.1082364 Medline

4. J. L. Yarger, G. H. Wolf, Chemistry: Polymorphism in liquids. *Science* **306**, 820 (2004). doi:10.1126/science.1104417 Medline

5. C. A. Angell, Insights into phases of liquid water from study of its unusual glass-forming properties. *Science* **319**, 582 (2008). doi:10.1126/science.1131939 Medline

6. G. N. Greaves, S. Sen, Inorganic glasses, glass-forming liquids and amorphizing solids. *Adv. Phys.* **56**, 1 (2007). doi:10.1080/00018730601147426

7. J. D. Bernal, A geometrical approach to the structure of liquids. *Nature* **183**, 141 (1959). doi:10.1038/183141a0

8. J. C. Phillips, Topology of covalent non-crystalline solids I: Short-range order in chalcogenide alloys. *J. Non-Cryst. Solids* **34**, 153 (1979). doi:10.1016/0022-3093(79)90033-4

9. W. K. Luo *et al*., Icosahedral short-range order in amorphous alloys. *Phys. Rev. Lett.* **92**, 145502 (2004). doi:10.1103/PhysRevLett.92.145502 Medline

10. J. C. Phillips, Topology of covalent non-crystalline solids II: Medium-range order in chalcogenide alloys and A□Si(Ge). *J. Non-Cryst. Solids* **43**, 37 (1981). doi:10.1016/0022-3093(81)90172-1

11. D. B. Miracle, A structural model for metallic glasses. *Nat. Mater.* **3**, 697 (2004). doi:10.1038/nmat1219 Medline

12. T. C. Hufnagel, Finding order in disorder. *Nat. Mater.* **3**, 666 (2004). doi:10.1038/nmat1227 Medline

13. P. S. Salmon, R. A. Martin, P. E. Mason, G. J. Cuello, Topological versus chemical ordering in network glasses at intermediate and extended length scales. *Nature* **435**, 75 (2005). doi:10.1038/nature03475 Medline

14. P. S. Salmon, A. C. Barnes, R. A. Martin, G. J. Cuello, Glass fragility and atomic ordering on the intermediate and extended range. *Phys. Rev. Lett.* **96**, 235502 (2006). doi:10.1103/PhysRevLett.96.235502 Medline

15. H. W. Sheng, W. K. Luo, F. M. Alamgir, J. M. Bai, E. Ma, Atomic packing and short-to-medium-range order in metallic glasses. *Nature* **439**, 419 (2006). doi:10.1038/nature04421 Medline

16. J. Haines *et al*., Topologically ordered amorphous silica obtained from the collapsed siliceous zeolite, silicalite-1-F: A step toward "perfect" glasses. *J. Am. Chem. Soc.* **131**, 12333 (2009). doi:10.1021/ja904054v Medline

17. D. Ma, A. D. Stoica, X. L. Wang, Power-law scaling and fractal nature of medium-range order in metallic glasses. *Nat. Mater.* **8**, 30 (2009). doi:10.1038/nmat2340 Medline

18. J. S. Tse, D. D. Klug, J. A. Ripmeester, S. Desgreniers, K. Lagarec, The role of non-deformable units in pressure-induced reversible amorphization of clathrasils. *Nature* **369**, 724 (1994). doi:10.1038/369724a0

19. G. N. Greaves *et al*., The rheology of collapsing zeolites amorphized by temperature and pressure. *Nat. Mater.* **2**, 622 (2003). doi:10.1038/nmat963 Medline

20. A. Navrotsky, Zeolites: Ordered, disordered, collapsed. *Nat. Mater.* **2**, 571 (2003). doi:10.1038/nmat969 Medline

21. H. W. Sheng *et al*., Polyamorphism in a metallic glass. *Nat. Mater.* **6**, 192 (2007). doi:10.1038/nmat1839 Medline

22. Q. S. Zeng *et al*., Origin of pressure-induced polyamorphism in $Ce_{75}Al_{25}$ metallic glass. *Phys. Rev. Lett.* **104**, 105702 (2010). doi:10.1103/PhysRevLett.104.105702 Medline

23. A. L. Greer, Metallic glasses. *Science* **267**, 1947 (1995). doi:10.1126/science.267.5206.1947 Medline

24. Materials and methods are available as supporting material on *Science* Online.

25. Q. S. Zeng *et al*., Substitutional alloy of Ce and Al. *Proc. Natl. Acad. Sci. U.S.A.* **106**, 2515 (2009). doi:10.1073/pnas.0813328106 Medline

26. The single crystal could also be viewed as an aggregate of polycrystals with the identical orientation; in either case, it reveals a LRO in the MG.

27. A. R. Yavari, Metallic glasses: The changing faces of disorder. *Nat. Mater.* **6**, 181 (2007). doi:10.1038/nmat1853 Medline

28. D. V. Louzguine-Luzgin, A. R. Yavari, G. Vaughan, A. Inoue, Clustered crystalline structures as glassy phase approximants. *Intermetallics* **17**, 477 (2009). doi:10.1016/j.intermet.2008.12.008

29. D. B. Miracle, T. Egami, K. M. Flores, K. F. Kelton, Structural aspects of metallic glasses. *MRS Bull.* **32**, 629 (2007). doi:10.1557/mrs2007.124

30. Y. Q. Cheng, E. Ma, H. W. Sheng, Atomic level structure in multicomponent bulk metallic glass. *Phys. Rev. Lett.* **102**, 245501 (2009). doi:10.1103/PhysRevLett.102.245501 Medline

31. Y. Ding *et al*., Zone-axis diffraction study of pressure-induced inhomogeneity in single-crystal Fe[sub 1−x]O. *Appl. Phys. Lett.* **87**, 041912 (2005). doi:10.1063/1.1999016

32. R. Boehler, New diamond cell for single-crystal x-ray diffraction. *Rev. Sci. Instrum.* **77**, 115103 (2006). doi:10.1063/1.2372734

33. J. Das *et al*., Plasticity in bulk metallic glasses investigated via the strain distribution. *Phys. Rev. B* **76**, 092203 (2007). doi:10.1103/PhysRevB.76.092203

34. H. W. Jin, Y. J. Kim, C. G. Park, *J. Mater. Sci.* **36**, 2089 (2001). doi:10.1023/A:1017567924939

35. Z. H. Huang, J. F. Li, Q. L. Rao, Y. H. Zhou, Effects of La content on the glass transition and crystallization process of Al–Ni–La amorphous alloys. *Intermetallics* **15**, 1139 (2007). doi:10.1016/j.intermet.2007.02.001

36. P. E. Blöchl, Projector augmented-wave method. *Phys. Rev. B* **50**, 17953 (1994). doi:10.1103/PhysRevB.50.17953

37. G. Kresse, J. Furthmüller, Efficiency of ab-initio total energy calculations for metals and semiconductors using a plane-wave basis set. *Comput. Mater. Sci.* **6**, 15 (1996). doi:10.1016/0927-0256(96)00008-0

38. G. Kresse, D. Joubert, From ultrasoft pseudopotentials to the projector augmented-wave method. *Phys. Rev. B* **59**, 1758 (1999). doi:10.1103/PhysRevB.59.1758

39. P. Brommer, F. Gähler, Potfit: Effective potentials from *ab initio* data. *Model. Simul. Mater. Sci. Eng.* **15**, 295 (2007). doi:10.1088/0965-0393/15/3/008

40. S. J. Plimpton, Fast parallel algorithms for short-range molecular dynamics. *J. Comput. Phys.* **117**, 1 (1995). doi:10.1006/jcph.1995.1039